JOURNAL OF SOLID STATE CHEMISTRY 71, 426–440 (1987)

Defect Structures in the Brannerite-Type Vanadates

VII. Preparation and Study of $Zn_{1-x}\emptyset_xV_{2-2x}Mo_{2x}O_6$ and $Zn_{1-x-y}\emptyset_xLi_yV_{2-2x-y}Mo_{2x+y}O_6$ Solid Solutions

KRZYSZTOF MOCAŁA AND JACEK ZIÓŁKOWSKI*

Institute of Catalysis and Surface Chemistry, Polish Academy of Sciences, 30-239 Krakow, ul. Niezapominajek, Poland

Received September 2, 1986; in revised form February 20, 1987

ZnV_2O_6 and $LiVMoO_6$, both of monoclinic brannerite-type structure, display miscibility in the whole range of composition and form the solid solution ZnLi = $Zn_{1-y}Li_yV_{2-y}Mo_yO_6$. ZnLi may be treated as a matrix able to incorporate an excess of Mo^{6+} ions compensated by the equivalent number of cation vacancies $\emptyset$ in the Zn^{2+} sublattice, which results in the formation of ZnLi$\emptyset$ = $Zn_{1-x-y}\emptyset_xLi_yV_{2-2x-y}Mo_{2x+y}O_6$. At $y = 0$, $x_{max} = 0.15$ and we deal with Zn$\emptyset$ = $Zn_{1-x}\emptyset_xV_{2-2x}Mo_{2x}O_6$ (which belongs to the ZnV_2O_6–MoO_3 system); at $y = 0.25$, $x_{max} \approx 0.30$, and at higher y, x_{max} diminishes again. Over the border of the existence of ZnLi$\emptyset$ several areas may be distinguished in which such phases coexist as saturated ZnLi$\emptyset$, MoO_3, V_2MoO_8, $ZnMoO_4$, and solid solution of MoO_3 in V_2O_5. Phase diagrams of ZnV_2O_6–MoO_3 and ZnV_2O_6–$LiVMoO_6$–MoO_3 systems are partly resolved on the basis of differential thermal analysis (DTA) and X-ray phase analysis. Lattice parameters of the above-mentioned solid solutions as a function of composition are determined. Comparative analysis of the data gathered for ZnLi$\emptyset$ and the formerly studied MnLi$\emptyset$ and Co$\emptyset$ leads to the following conclusions. The MeV_2O_6 lattices are amenable to substitution of Mo^{6+} for V^{5+} in a quantity exceeding 50%. The "solubility" of vacancies is strongly dependent on the kind of Me^{2+} in the matrix. The synergetic effect linked with the simultaneous presence of Zn^{2+} and Li^+, manifested by negative deviations from Vegard's law, increases the stability of the matrix and its capacity to create vacancies (cf. x_{max} at $y = 0$ and $y = 0.25$). Dopant ions of various sizes influence the values of lattice parameters. Parameters a and b are dependent on the Mo/V ratio and practically insensitive to the occupation of the original Me^{2+} site. Parameter c (or $c \sin \beta$) is almost sensitive only to the size of $Me^{2+}/Li^+/\emptyset$. Cation vacancies behave as ions of a size smaller than the exhausted cations by at least 0.01 Å but rather close to 0.06 Å.

Introduction

In the present series of investigations (*1–6*) we have focused our attention on the solid solutions of MoO_3 and Li_2O in the matrices of bivalent metal vanadates MeV_2O_6 crystallizing in the brannerite-type structure (Fig. 1) (*1, 7, 8*). Previously we have found solid solutions described by the formulae:

Me$\emptyset$ type

$Mn_{1-x}\emptyset_xV_{2-2x}Mo_{2x}O_6$, $0 \le x \le 0.45$ (*1, 2, 4*)

$Co_{1-x}\emptyset_xV_{2-2x}Mo_{2x}O_6$, $0.02 \le x \le 0.22$ (*6*)

MnLi$\emptyset$ type

$Mn_{1-x-y}\emptyset_xLi_yV_{2-2x-y}Mo_{2x+y}O_6$, $0 \le x \le 0.45$, $0 \le y \le 1$ (*5*)

* To whom all correspondence should be addressed.

0022-4596/87 $3.00

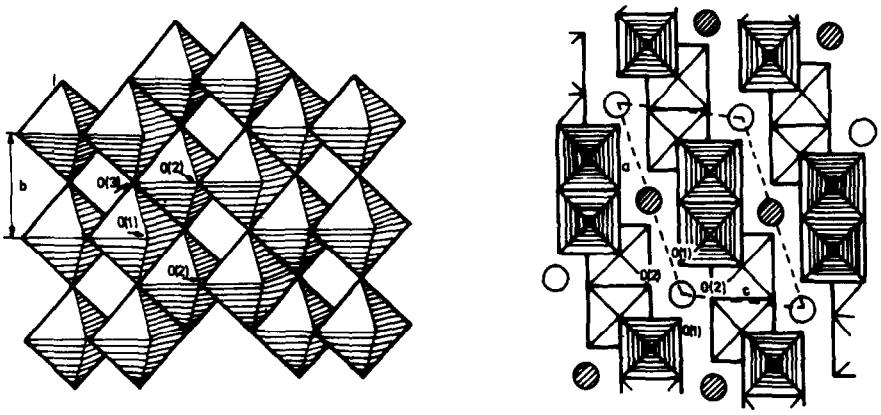

FIG. 1. Idealized presentation of the brannerite-type structure MeV_2O_6 (after (7)). (a) A sheet of VO_6 octahedra parallel to the (001) plane. (b) Projection of the structure on the (010) plane with Me^{2+} cations and VO_6 octahedra on two levels, distinguished by dashing.

CuCuØ type

$$Cu^{2+}_{1-x-y}Ø_xCu^{+}_yV_{2-2x-y}Mo_{2x+y}O_6,$$
$$0 \le x \le 0.23,\ 0 \le y \le 0.27 \quad (3)$$

In these solutions Mo^{6+} ions are substituted randomly for V^{5+} and charge compensation is accomplished by an equivalent number of cationic vacancies Ø at the bivalent metal site, by a partial reduction of the bivalent metal, or by replacing the bivalent metal with a Li^+ ion, Me^{2+}, Me^+, Li^+, and Ø being distributed statistically in *Me* positions. It may be worth recalling that *Me*Ø solutions are not formed for *Me* = Mg, Cd (*1*). As it is known from the literature (*9*, *10*), *Me* positions in the brannerite-type matrix may be entirely filled up with monovalent cations, with simultaneous equivalent substitution of Mo^{6+} for V^{5+} ($LVMoO_6$) and a further increase of the Mo^{6+}/V^{5+} ratio result in a deficiency of the monovalent cations:

*L*Ø type

$$L_{1-x}Ø_xV_{1-x}Mo_{1+x}O_6,$$
$$L = \text{Li}, \quad 0 \le x \le 0.16$$
$$L = \text{Na}, \quad 0 \le x \le 0.30$$
$$L = \text{K}, \quad 0.18 \le x \le 0.24$$
$$L = \text{Ag}, \quad 0 \le x \le 0.12$$

The *L*Ø formulae may be derived from *MeL*Ø at $x + y = 1$.

In the present paper, our studies are extended onto the $Zn_{1-x}Ø_xV_{2-2x}Mo_{2x}O_6$ and $Zn_{1-x-y}Ø_xLi_yV_{2-2x-y}Mo_{2x+y}O_6$ solid solutions which consequently will be labeled throughout the paper as ZnØ–*X* and ZnLiØ–*XY* ($X = 100x$, $Y = 100y$), respectively, or briefly as ZnØ and ZnLiØ when it is not necessary to indicate the composition.

The composition of ZnØ may be expressed as $Zn_{1-x}Ø_xV_{2-2x}Mo_{2x}O_6 = (1 - x)ZnV_2O_6 + 2xMoO_3$ which indicates that this solution is localized along the ZnV_2O_6–MoO_3 section of the ZnO–V_2O_5–MoO_3 diagram (Fig. 2a). Similarly, the composition of ZnLiØ may be expressed as $Zn_{1-x-y}Ø_xLi_yV_{2-2x-y}Mo_{2x+y}O_6 = (1 - x - y)ZnV_2O_6 + yLiVMoO_6 + 2xMoO_3$ which indicates that this solution is localized in the ZnV_2O_6–$LiVMoO_6$–MoO_3 plane of the quaternary ZnO–Li_2O–V_2O_5–MoO_3 system (Figs. 2b and 2c). It has been found convenient to represent the composition of the pseudo-

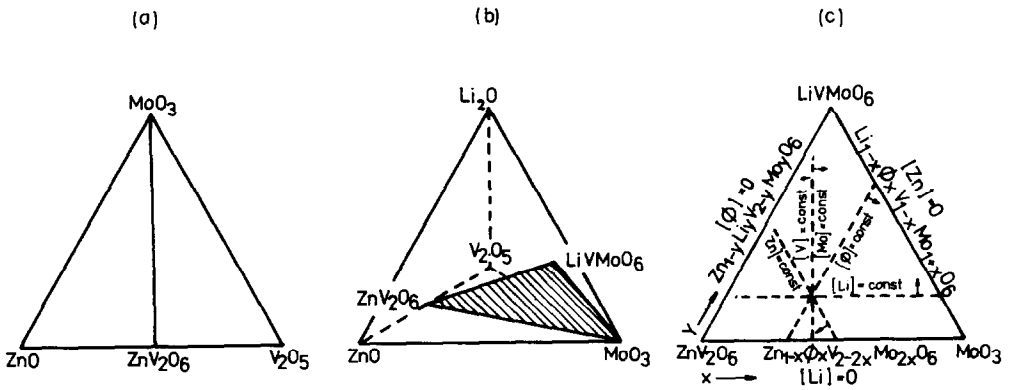

FIG. 2. Localization of the studied solid solutions in the respective composition diagrams. (a) $Zn\emptyset$ = $Zn_{1-x}\emptyset_xV_{2-2x}Mo_{2x}O_6$ solid solution lies along the ZnV_2O_6–MoO_3 section of the ZnO–V_2O_5–MoO_3 system. (b) Composition of $ZnLi\emptyset$ = $Zn_{1-x-y}\emptyset_xLi_yV_{2-2x-y}Mo_{2x+y}O_6$ solid solution falls within the ZnV_2O_6–$LiVMoO_6$–MoO_3 section of the ZnO–V_2O_5–MoO_3–Li_2O system. (c) Properties of the equilateral composition triangle ZnV_2O_6–$LiVMoO_6$–MoO_3. Arrow mark the directions in which the concentration of the indicated component increases.

ternary ZnV_2O_6–$LiVMoO_6$–MoO_3 system by means of the equilateral triangle configuration, formally using the $ZnLi\emptyset$ formula over its whole area. Consequently, composition variables X and Y are used to express the composition along the ZnV_2O_6–MoO_3 and ZnV_2O_6–$LiVMoO_6$ sides of the triangle, respectively. The characteristics of such a diagram are shown in Fig. 2c. In particular, the series of samples of a constant concentration of Zn, Li, V, Mo, and $\emptyset$ can be easily found as lying on the respective straight lines.

In this paper the existence of $Zn\emptyset$ and $ZnLi\emptyset$ solid solutions is confirmed, their stability ranges are determined, and the T–ZnV_2O_6–MoO_3 and T–ZnV_2O_6–$LiVMoO_6$–MoO_3 phase diagrams are partially resolved.

Experimental

The $Zn\emptyset$ and $ZnLi\emptyset$ solid solutions were synthesized using the amorphous citrate precursors (*11*), as adapted for our systems and described in Ref. (*5*). In the case of $Zn\emptyset$ and $ZnLi\emptyset$ the starting materials were water solutions of $Zn(NO_3)_2$ and Li_2CO_3, NH_4VO_3, and $(NH_4)_2Mo_7O_{24} \cdot 4H_2O$, all of p.a. grade. The final thermal treatment of ZnO samples in air is given in Table I. Final calcinations of $ZnLi\emptyset$ samples were 500–570°C for 60 hr, adjusted so as to avoid the melting. Samples exhibiting, in the X-ray analysis, the presence of phases other than a brannerite one were additionally heated at the same temperature for 100 hr, and periodically tested by X-ray analysis, to make sure that real equilibrium had been reached. After annealing, samples were quenched to room temperature, to freeze the high-temperature equilibrium state. X-ray analysis showed the formation of pure ZnV_2O_6 or $Zn\emptyset$ for samples with $0 \leq X \leq 12.5$ and $Y = 0$. Samples with a higher content of MoO_3 exhibited the presence of $ZnMoO_4$, V_2MoO_8, and MoO_3, and a solid solution of MoO_3 in V_2O_5 (labeled V*M*) which is believed to be $V^{5+}_{2-2y}V^{4+}_yMo^{6+}_yO_5$ (*12*). It will be shown further that, in view of differential thermal analysis (DTA) (Fig. 3) and the changes of lattice parameters with composition (Fig. 5), the solubility limit of MoO_3 in ZnV_2O_6 corresponds to $X = 15$, in spite of the fact

TABLE I

FINAL THERMAL TREATMENT AND PHASE COMPOSITION OF SAMPLES BELONGING TO THE ZnV_2O_6–MoO_3 SYSTEM

$X = 100x$	Calcination conditions[a]	Color	Phase composition
0	H	Yellow	ZnV_2O_6
2.5	S_1	Yellow	ZnØ
5	S_1	Yellow	ZnØ
7.5	S_1	Yellow	ZnØ
10	S_1	Yellow	ZnØ
12.5	S_1	Olive-yellow	ZnØ
15	S_2	Olive-green	ZnØ + (V*M* + $ZnMoO_4$) traces
17.5	S_2	Olive	ZnØ + V*M* + $ZnMoO_4$
20	S_2	Olive	ZnØ + V*M* + $ZnMoO_4$
25	S_2	Olive	$ZnMoO_4$ + V*M* + ZnØ
30	S_3	Olive	$ZnMoO_4$ + V*M* + ZnØ
35	S_3	Olive	$ZnMoO_4$ + V*M* + ZnØ
40	S_3	Brown-green	$ZnMoO_4$ + V*M* + V_2MoO_8
46	S_3	Brown-green	V_2MoO_8 + $ZnMoO_4$ + V*M*
50	S_3	Brown-green	V_2MoO_8 + $ZnMoO_4$ + (V_2O_5 + MoO_3) traces
54	S_3	Gray	V_2MoO_8 + $ZnMoO_4$ + MoO_3
68	S_3	Gray	V_2MoO_8 + MoO_3 + $ZnMoO_4$
76	S_3	Gray-green	MoO_3 + V_2MoO_8 + $ZnMoO_4$

[a] H, 600°C/ 20 hr + 2 × 600°C/50 hr; S_1, 570°C/40 hr + 580°C/100 hr; S_2, 580°C/60 hr + 580°C/ 100 hr; S_3, 500°C/70 hr + 550°C/140 hr + 570°/95 hr.

that the sample of nominal composition ZnØ–15 contained traces of nonbrannerite phases which could segregate on cooling. As for the ZnV_2O_6–$LiVMoO_6$–MoO_3 system the miscibility of ZnV_2O_6 and $LiVMoO_6$ has been observed in the whole range of composition, resulting in the formation of ZnLi = $Zn_{1-y}Li_yV_{2-y}Mo_yO_6$ solid solutions (ZnLiØ with $X = 0$). After the incorporation of an excess of MoO_3, ZnLi became ZnLiØ until the border (Fig. 4) corresponded to the mutually dependent X_{max} and Y_{max}. Beyond this border the samples exhibited the presence of the excess phases as indicated above for the ZnV_2O_6–MoO_3 system. As shown in (*5*) and mentioned in the introduction samples lying along the $LiVMoO_6$–MoO_3 side of the diagram were composed of LiØ until X_{max} = 16 and were mixtures of LiØ + MoO_3 above X_{max}.

The X-ray diffraction patterns were obtained with a DRON-2 diffractometer using Cu$K\alpha$ radiation. Phase identification was based upon published patterns of ZnV_2O_6 (*13–15*), $ZnMoO_4$ (*16*), V_2MoO_8 (*17*), and MoO_3 (*18*). Determination of the lattice parameters, DTA (Setaram M5 microanalyzer), elemental analysis (Pye-Unicam FP-90 spectrometer), and EPR measurements were carried out in the same way as was described in earlier works (*5*, *6*).

Results

Verification of the ZnØ and ZnLiØ Formulae

The elemental analyses of the chosen samples, performed after the final thermal treatment, proved a stoichiometry corresponding to the assumed ZnØ and ZnLiØ formulae within the error of the analytical

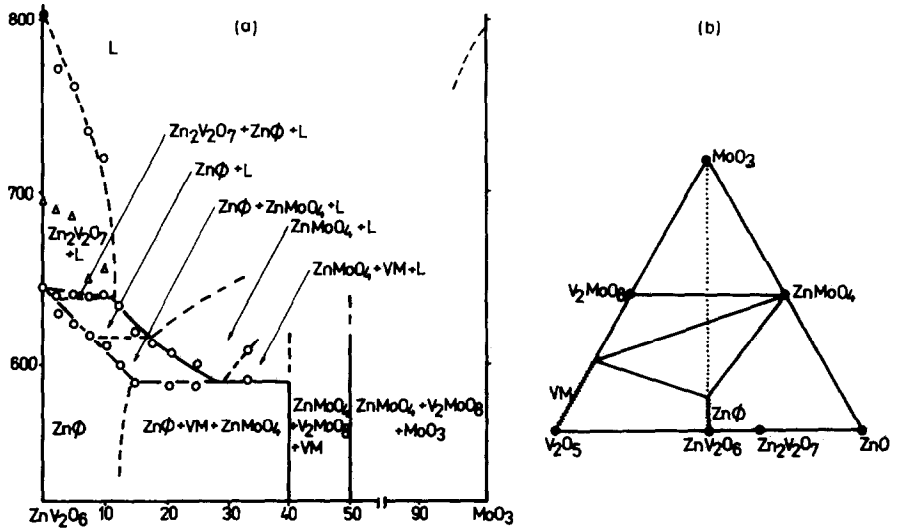

FIG. 3. (a) T–ZnV_2O_6–MoO_3 slice of the T–ZnO–V_2O_5–MoO_3 phase diagram. (b) Subsolidus portion of the phase diagram of the ternary ZnO–V_2O_5–MoO_3 system divided into natural subdiagrams. Zn∅ = $Zn_{1-x}\emptyset_xV_{2-2x}Mo_{2x}O_6$, and VM = $V^{5+}_{2-2y}V^{4+}_yMo^{6+}_yO_5$, the lines along which these solutions exist are dashed.

method which means that there was no loss of material during preparation. The X-ray phase analyses have shown single brannerite-type phases, with some reflections (especially those of $k = 0$) being increasingly shifted along the series, which proves that the solid solutions were formed. In principle, the charge compensation could be accomplished in other ways, e.g., $Zn^{2+}V^{5+}_{2-2x}V^{4+}_xMo^{6+}_xO_6$ and $Zn^{2+}V^{5+}_{2-x}Mo^{5+}_xO_6$ in the ZnV_2O_6–MoO_3 system or $Zn^{2+}_{1-y}Li^+_yV^{5+}_{2-x-y}Mo^{6+}_yMo^{5+}_xO_6$ and $Zn^{2+}_{1-y}Li^+_yV^{5+}_{2-2x-y}V^{4+}_xMo^{6+}_{x+y}O_6$ in the ZnV_2O_6–$LiVMoO_6$–MoO_3 system. However, these hypothetical compositions do not correspond to the stoichiometry observed. Had these hypothetical solutions been formed, a part of the material should have remained as excess phases which could have been easily detected with X-rays (cf. an analogous discussion in Refs. (*5*, *6*)). Nor have any EPR spectra been observed for ZnV_2O_6, Zn∅, and ZnLi∅. An EPR signal of the shape and position similar to those reported by Robb *et al.* (*12*) was observed only for samples of $12.5 \leq X \leq 40$ and $0 \leq Y \leq 30$, which may be ascribed to V^{4+} in VM, the phase also detected in the X-ray analysis in this range of composition.

Phase Diagrams

The data listed in Table I together with additional observations resulting from DTA and X-ray analysis (as already mentioned under Experimental) clearly indicate that the Zn∅ solution exists in the ZnV_2O_6–MoO_3 system in the range $0 \leq X \leq 15$. An increase of the MoO_3 content over $X_{max} = 15$ leads to three subsequent regions in the subsolidus: Zn∅–X_{max} + $ZnMoO_4$ + VM, $ZnMoO_4$ + VM + V_2MoO_8, and $ZnMoO_4$ + V_2MoO_8 + MoO_3 (Fig. 3a). This gives rise to the natural subdiagrams of the T–ZnO–V_2O_5–MoO_3 diagram shown in Fig. 3b. The division is similar to that found for CoO–V_2O_5–MoO_3 system (*6*) and entirely different from that observed for MnO–V_2O_5–MoO_3

(*1*).[1] The division of quadrilateral fields V*M*–ZnØ and ZnØ–$ZnMoO_4$–ZnO into subdiagrams is not discussed in this paper. The above results clearly show that T–Zn V_2O_6–MoO_3 is an arbitrary slice of T–ZnO–V_2O_5–MoO_3. The composition of the phases coexisting along the ZnV_2O_6–MoO_3 line cannot be expressed on this composition scale; the discussed slice is pierced by the respective tie-lines. The shape of a part of the T–ZnV_2O_6–MoO_3 slice (Fig. 3a) has been established by DTA. ZnV_2O_6 melts incongruently at 645°C. ZnØ samples melt between 645 and 590°C, depending on the composition. There is a ternary eutectic between ZnØ–X_{max}, $ZnMoO_4$, and V*M*, melting at 590°C. A small difference of only 55°C between the melting points of ZnV_2O_6 and the ternary eutectic apparently obscured (except for one sample) any distinct DTA effect corresponding to the melting point of the binary eutectic between $ZnMoO_4$ and ZnØ-X_{max}. Its position was thus estimated to be 620°C and is marked with a dashed line. The liquidus line between $Zn_2V_2O_7$ + liquid and liquid areas was determined from both heating and cooling DTA runs (circles and triangles in Fig. 3a, respectively). The differences between the two sets of data are very large.

According to Clark and Pick (*28*), Chaplina (*29*), Markarov *et al.* (*30*), and Brown and Hummel (*31*) the liquidus line is crossed over pure ZnV_2O_6 at 862, 720, 700, and 800°C, respectively, while our data give 810°C. These discrepancies seem to be due to an abrupt fall of the liquidus line in the ZnO–V_2O_5 diagram (*29–31*) and possible small variations in the composition of samples due to the evaporation of one component from the melt in course of DTA and deviation from stoichiometry (*15*).

Figure 4 shows the subsolidus portion of the pseudoternary ZnV_2O_6–$LiVMoO_6$–MoO_3 phase diagram as determined by X-ray phase analysis of the frozen samples. The range of stability of the brannerite-type ZnLiØ solid solution extends over about 40% of the area of the triangle. The remaining parts correspond to the multiphase areas. ZnLiØ–X_{max}–MoO_3 is the only area which includes phases that build up the system. In other areas, phases belonging to the quaternary ZnO–Li_2O–V_2O_5–MoO_3 system were found to coexist, which points to the fact that ZnV_2O_6–$LiVMoO_6$–MoO_6 is also an arbitrary subsystem of the indicated quaternary system. The areas of coexistence of various phases were tentatively "projected" from a multidimensional T–ZnO–Li_2O–V_2O_5–MoO_3 diagram onto the ZnV_2O_6–$LiVMoO_6$–MnO_3 plane as marked with dotted lines in Fig. 4. The areas found are

[1] A doubt may arise whether V_2MoO_8 or $V_9Mo_6O_{40}$ exist in the ZnO–V_2O_5–MoO_3 and CoO–V_2O_5–MoO_3 systems. As already pointed out in Ref. (*6*) the T–V_2O_5–MoO_3 diagram has been the subject of numerous works (*19–23*) and either V_2MoO_8 or $V_9Mo_6O_{40}$ has been indicated as the compound formed in the system. However, it is evident that $V_9Mo_6O_{40} = 4V_2O_5 \cdot VO_2 \cdot 6MoO_3$ is reduced and does not belong to the V_2O_5–MoO_3 system. Depending on the experimental conditions, various phases, including solid solutions, of various valence states of cations can be certainly formed in the V–Mo–O system; in addition to V_2MoO_6 and $V_9Mo_6O_{40}$, $V_6Mo_4O_{25}$ (*24*), $VMoO_5$ (*25*), VMo_2O_{8+x}, and VMo_3O_{11} (*26, 27*) also have been described. However, elucidation of the whole V–Mo–O system is not the aim of the present studies. According to our results (*6*) and literature data (*26*), under the oxidative conditions (air), V_2MoO_8 of the crystallographic characteristic, remaining in agreement with Ref. (*17*), is formed in the V_2O_5–MoO_3 system. V_2MoO_8 melts congruently at 630°C and forms two eutectics with MoO_3 (600°C, 60 mole% MoO_3) and with V*M* (628°C, 47 mole% MoO_3) (*6*). Experimental results obtained in the present and in the former works (*6*) for the ternary *Me*O–V_2O_5–MoO_3 (*Me* = Co, Zn) remain in agreement with the above finding. They clearly demonstrate that the *Me*MoO_4–V_2MoO_8 straight line is one of lines dividing the ternary system into natural subsystems. Samples lying on this line are composed of *Me*MoO_4 + V_2MoO_8; samples of higher MoO_3 content contain *Me* MoO_4 + V_2MoO_8 + MoO_3; samples of lower MoO_3 content include *Me*MoO_4 + v_2MoO_6 + V*M*. Thus the appearance/disappearance boundary of V*M*/MoO_3 points to the phase containing V_2O_5 and MoO_3 in the molar ratio 1 : 1.

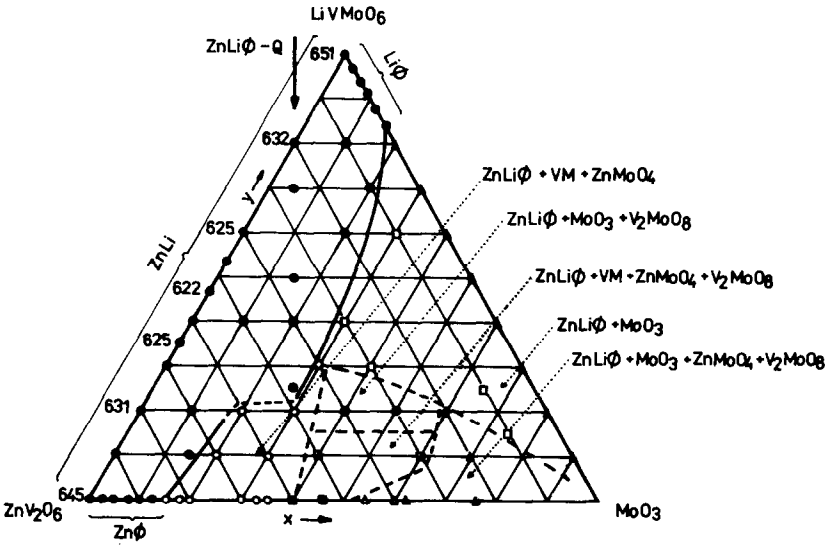

FIG. 4. Subsolidus portion of the phase diagram of the pseudoternary ZnV_2O_6–$LiVMoO_6$–MoO_3 system, based on X-ray phase analysis. Numbers give the melting points determined by DTA. Symbols used are explained in Figs. 2 and 3. The arrow marks the line along which ZnLiØ–*Q* samples are localized. Studied samples of the indicated, differentiated phase composition are distinguished by points of various shapes. Black circles correspond to samples composed of single brannerite-type phase ZnØ, ZnLi, LiØ, and ZnLiØ in the field of triangle.

ZnLiØ + MoO_3, ZnLiØ + MoO_3 + V_2MoO_8, ZnLiØ + MoO_3 + V_2MoO_8 + $ZnMoO_4$, ZnLiØ + V_2MoO_8 + $ZnMoO_4$ + V*M*, and ZnLiØ + $ZnMoO_4$ + V*M*.

X-Ray Studies of ZnV_2O_6 and ZnØ, ZnLiØ, ZnLi Solid Solutions

X-ray patterns of ZnV_2O_6 and ZnØ-12.5 are given in Table II. In Table III the lattice parameters for these two samples are listed and compared with those determined by Angenault and Rimsky (*14*) and by Andreetti *et al.* (*15*) for single crystals of ZnV_2O_6. ZnV_2O_6 and ZnØ grains orient easily. Therefore, like for α-CoV_2O_6 and α-CoØ (*6*), we were unable to obtain reliable intensity data even when using a special technique described in Ref. (*1*).

Lattice parameters for other ZnØ samples are presented in Fig. 5 and compared with the data for MnØ and CoØ (*1, 6*). It can be seen that increasing *X* in ZnØ from 0 to 15 results in a linear increase of *a*, *b*, and *V* by $\Delta a = 0.40\%$, $\Delta b = 0.94\%$, $\Delta V = 1.00\%$. The other parameters change in a monotonal but nonlinear manner by $\Delta c = -0.17\%$, $\Delta c \sin\beta = -0.34\%$, $\Delta\beta = 0.23\%$.

Figure 6 shows the changes of the lattice parameters of ZnLi solid solutions between ZnV_2O_6 and $LiVMoO_6$ together with those reported earlier for MnLi (*5*). In this case increasing *Y* in ZnLi–*Y* from 0 to 1 (i.e., from ZnV_2O_6 to $LiVMoO_6$) results in a linear increase of *a* and *b* by $\Delta a = 1.06\%$ and $\Delta b = 3.29\%$. The other parameters change in a nonlinear manner by $\Delta c = 0.99\%$, $\Delta c \sin\beta = 0.95\%$, $\Delta\beta = 0.35\%$, and $\Delta V = 5.16\%$.

Figure 7 presents the lattice parameters for a series of ZnLiØ–*XY* solutions with (*X*, *Y*) equal to (0, 80), (5, 75), (15, 50), (20, 40), (27.5, 25), chosen in such a way that the concentration of vanadium (2 − 2*X* − *Y*) and molybdenum (2*X* + *Y*) is constant

TABLE II

X-RAY POWDER DATA FOR ZnV_2O_6 AND $Zn\emptyset-12.5$

	ZnV_2O_6			$Zn\emptyset-12.5$			
$h\,k\,l$	d_{obs} (Å)	d_{cal} (Å)	I	d_{obs} (Å)	d_{cal} (Å)	I	$h\,k\,l$
0 0 1	6.12	6.12	vw	6.10	6.10	m	0 0 1
2 0 $\bar{1}$	4.35	4.34	m	4.35	4.36	m	2 0 $\bar{1}$
2 0 0	4.31	4.30	w	4.30	4.31	w	2 0 0
1 1 0	3.265	3.264	m	3.288	3.288	m	1 1 0
2 0 $\bar{2}$	3.079	3.079	s	3.082	3.081	s	2 0 $\bar{2}$
1 1 $\bar{1}$	3.060	3.061	w		3.081		1 1 $\bar{1}$
0 0 2		3.060			3.049		0 0 2
2 0 1	3.036	3.038	vs	3.033	3.032	vs	2 0 1
1 1 1	2.727	2.728	m	2.738	2.738	m	1 1 1
1 1 $\bar{2}$	2.403	2.404	w	2.410	2.411	w	1 1 $\bar{2}$
3 1 $\bar{1}$	2.312	2.312	s	2.323	2.325	m	3 1 $\bar{1}$
4 0 $\bar{1}$		2.310			2.317		4 0 $\bar{1}$
3 1 0	2.227	2.226	m	2.235	2.235	w	3 1 0
2 0 $\bar{3}$	2.170	2.175	m	2.178	2.178	w	4 0 $\bar{2}$
4 0 $\bar{2}$		2.171			2.173		2 0 $\bar{3}$
4 0 0	2.152	2.152	m	2156	2.155	w	4 0 0
2 0 2		2.151		2.144	2.144	m	2 0 2
3 1 $\bar{2}$	2.105	2.105	m	2.115	2.115	w	3 1 $\bar{2}$
1 1 2	2.093	2.093	w	2.094	2.094	w	1 1 2
0 0 3	2.040	2.040	s	2.033	2.033	s	0 0 3
3 1 1	1.925	1.924	m	1.928	1.928	m	3 1 1
4 0 $\bar{3}$	1.857	1.856	m	1.859	1.860	m	4 0 $\bar{3}$
1 1 $\bar{3}$	1.848	1.849	m	1.849	1.849	m	1 1 $\bar{3}$
0 2 0	1.763	1.764	m	1.779	1.779	m	0 2 0
2 0 $\bar{4}$	1.642	1.643	m		1.647		2 2 $\bar{1}$

while the concentration of vacancies (X) increases along this series following the substitution of Zn^{2+} for Li^+. Because the sizes of Zn^{2+} and Li^+ are comparable, the data found for this series of samples (labeled $ZnLi\emptyset$–Q) will be used under Discussion to determine the "size" of the cation vacancy. The compositions of $ZnLi\emptyset$–Q samples are localized along a vertical line in Fig. 4 and are marked there by an arrow. Increasing the concentration of vacancies (X) from 0 to 27.5 in $ZnLi\emptyset$–Q results in a linear decrease of b, β, and V by $\Delta b = -0.25\%$, $\Delta\beta = -0.04\%$, $\Delta V = -0.45\%$ and a nonlinear decrease of c and $c \sin\beta$ by $\Delta c = -0.18\%$ and $\Delta c \sin\beta = -0.14\%$. Parameter a is constant along this series of samples.

Table IV summarizes the relative changes of the main lattice parameters in various solid solutions of the brannerite-type structure studied so far, corresponding to the substitution of 0.1 Mo^{6+} for 0.1 V^{5+}, labeled $\Delta p_{0.1}$, where p is a general symbol of parameters. Calculated $\Delta p_{0.1}$, as described under Discussion, are also included in Table IV.

Discussion

The observed relative changes of all cell dimensions of $Zn\emptyset$, ZnLi, and $ZnLi\emptyset$ as well as those of the previously studied $Mn\emptyset$, MnLi, and $Co\emptyset$ solid solutions can be accounted for by the specific details of the brannerite-type structure and the differences in cationic radii r_z (Table V), as taken from the set proposed by one of us (*32*). Because the ionic radii from Ref. (*32*) differ slightly from those listed by Shannon (*33*) r_s, the latter are also included in Table V and will be used below for some comparative calculations.

In the MeV_2O_6 structure (Fig. 1 (*7, 13*)), VO_6 octahedra sharing opposite corners form chains parallel to the b axis. The

TABLE III

UNIT CELL PARAMETERS FOR ZnV_2O_6 AND $Zn\emptyset-12.5$

	ZnV_2O_6			$Zn\emptyset-12.5$
Parameter	Ref. (*14*)	Ref. (*15*)[a]	Present work	(present work)
a (Å)	9.242(8)[b]	9.2651(9)	9.240(3)	9.270(2)
b (Å)	3.526(3)	3.5242(5)	3.528(1)	3.557(1)
c (Å)	6.574(6)	6.5889(8)	6.571(3)	6.560(2)
β (deg)	111.55(5)	111.37(1)	111.36(2)	111.61(1)
$c \sin\beta$ (Å)	6.114(6)	6.1359(8)	6.120(3)	6.098(2)
V (Å^3)	199.25	200.34	199.5	201.1

[a] Sample contained 3% of V^{4+}.
[b] Estimated standard deviation.

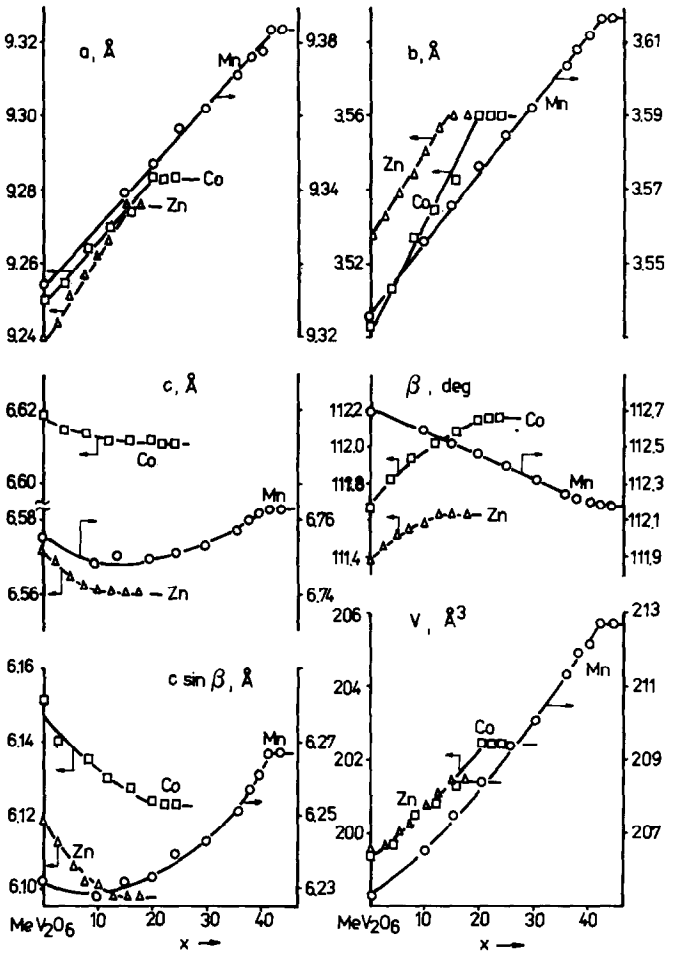

FIG. 5. Unit cell parameters vs $X = 100x$ for $Me\emptyset = Me_{1-x}\emptyset_x V_{2-2x}Mo_{2x}O_6$, Me = Mn, Co, and Zn (estimated standard deviation is usually 0.001, 0.002, and 0.003 Å for b, c and a, respectively, and 0.02° for β).

lengths[2] of the –V–O(3)–V–O(3)–V– bonds nearly aligning the b axis are 1.83 Å. VO_6 octahedra of the adjacent chains share edges in the [100] direction, thus forming anionic sheets parallel to the (001) plane. Double –V–O(2)–V– bridges along the a axis are composed of bonds alternating between 1.68 and 2.54 Å, which indicates that the structure is much more loosely packed in the [100] direction than in the [010] one. The Me^{2+} ions are situated between the anionic sheets; MeO_6 octahedra sharing the opposite edges form chains paralleling the b axis and are not linked to each other.

The expected influence of dopant ions of differentiated ionic radii (or of vacancies) on the lattice parameters may be estimated by simple geometrical calculations by considering the sizes of regular octahedra in the following manner:

[2] The sets of V–O bond lengths in various MeV_2O_6 compounds of the brannerite-type structure are nearly the same. The values quoted here concern the structure of ZnV_2O_6 (*13*).

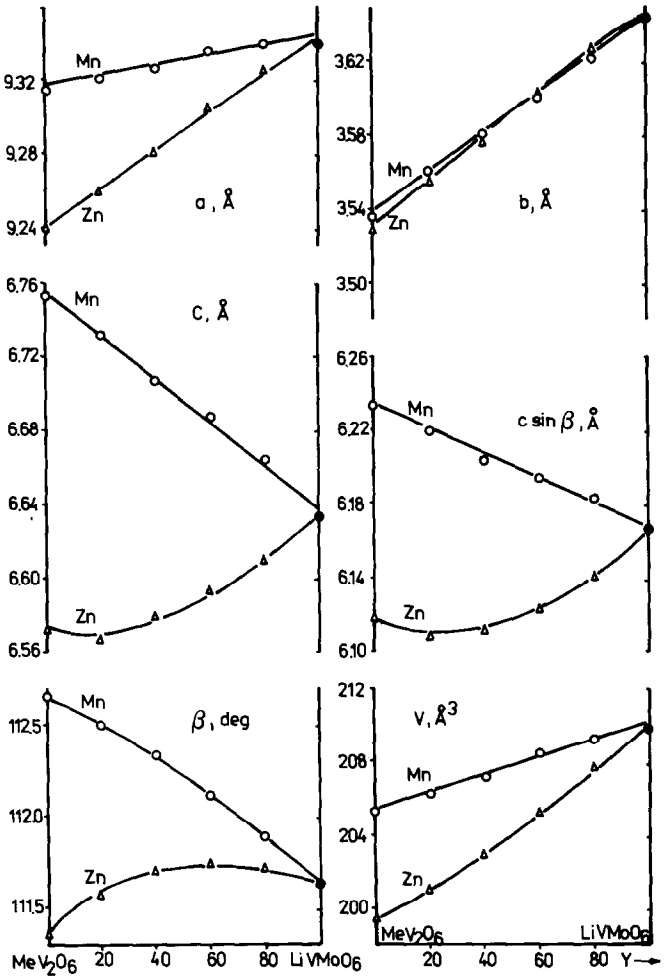

FIG. 6. Unit cell parameters vs $Y = 100y$ for $MeLi = Me_{1-y}Li_yV_{2-y}Mo_yO_6$, Me = Mn, Zn.

(i) Parameter b should depend either on the distance between the opposite corners of a BO_6 octahedron (B = V, Mo) or on the distance between the opposite edges of an AO_6 octahedron (A = Me, Li, ∅).

(ii) Parameter a should depend on the distance between opposite edges of BO_6. Because AO_6 chains do not touch each other along the a axis, occupation of A site by Me/Li/∅ may have only a minor and indirect influence on parameter a.

(iii) Parameter $c \sin \beta$, expressing the distance between the anionic (001) layers, should depend on the sum of the distances between the opposite corners of BO_6 and opposite faces of AO_6.

Let us first consider the results obtained for ZnLi∅–Q series of samples to evaluate the size of the cation vacancy. The compositions of the first and the last samples of this series are described by the formulae $Zn_{0.2}Li_{0.8}∅_0V_{1.2}Mo_{0.8}O_6$ and $Zn_{0.475}Li_{0.25}∅_{0.275}V_{1.2}Mo_{0.8}O_6$, which means that the V/Mo ratio, the occupation of BO_6 octahedra, and their sizes are constant while

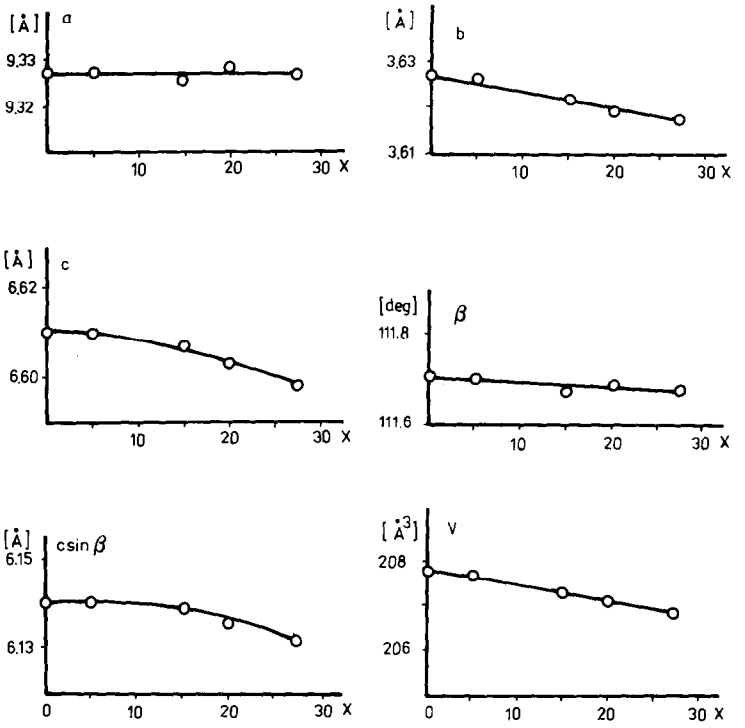

FIG. 7. Unit cell parameters vs $X = 100x$ for ZnLiØ–Q series of solid solutions of constant V/Mo ratio (cf. text and Fig. 4).

TABLE IV

EXPERIMENTAL AND CALCULATED RELATIVE CHANGES OF THE LATTICE PARAMETERS (IN %) FOR VARIOUS BRANNERITE-TYPE SOLID SOLUTIONS CORRESPONDING TO THE SUBSTITUTION OF 0.1 Mo^{6+} FOR 0.1 V^{5+}

						Calculated from the size of BO_6	
	ZnLi	MnLi	ZnØ	MnØ	CoØ	r_z	r_s
			Experimental				
$\Delta a_{0.1}$	0.106	0.025	0.133	0.085	0.081	0.090	0.131
$\Delta b_{0.1}$	0.329	0.305	0.313	0.273	0.363	0.090	0.131
$\Delta c \sin \beta_{0.1}$	0.095	−0.109	−0.113	−0.032	−0.105		
$\Delta V_{0.1}$	0.516	0.219	0.333	0.414	0.341		
			Calculated from the size of AO_6 and the indicated r_z or r_s				
$\Delta b_{0.1}$ (r_z)	−0.127	−0.434	−0.144	−0.139	−0.145		
$\Delta b_{0.1}$ (r_s)	0.095	−0.320	−0.031	−0.030	−0.031		
			Calculated from the sizes of AO_6 and BO_6 and the indicated r_z or r_s				
$\Delta c \sin \beta_{0.1}$ (r_z)	0.002	−0.126	−0.003	−0.003	−0.005		
$\Delta c \sin \beta_{0.1}$ (r_s)	0.119	−0.047	0.069	0.068	0.069		
			Calculated as above assuming that the size of BO_6 is independent on doping				
$\Delta c \sin \beta_{0.1}$ (r_z)	0.055	−0.071	−0.059	−0.058	−0.059		
$\Delta c \sin \beta_{0.1}$ (r_s)	0.199	0.032	−0.011	−0.011	−0.011		

TABLE V

IONIC RADII

Ion	Coordination	Radius after (*32*) r_z (Å)	Radius after (*33*) r_s (Å)
Mn^{2+}	VI	0.823	0.83
Co^{2+}	VI	0.734	0.745
Zn^{2+}	VI	0.755	0.74
Li^{+}	VI	0.728	0.76
V^{5+}	VI	0.465	0.54
Mo^{6+}	VI	0.498	0.59
O^{2-}	III	1.363	1.36

Li^+ ions are replaced by Zn^{2+} and ∅ with the stoichiometry $0.55Li^+ \rightarrow 0.275Zn^{2+} + 0.275\emptyset$. It results from the values of the ionic radii r_z that the face–face distances in LiO_6 and ZnO_6 octahedra are 2.414 and 2.446 Å, respectively, the difference being 0.032 Å. Taking into account that only 27.5% of *A* sites are filled with Zn^{2+} along the series of samples and assuming momentarily that the "radius" of ∅ is the same as that of Li^+ we arrive at the conclusion that the parameter $c \sin \beta$ should increase by 0.009 Å. In fact (Fig. 7) it decreases by 0.010 Å. The smaller radius of ∅ seems to be the only cause responsible for the difference of 0.009 + 0.010 = 0.019 Å. The fact that all lattice parameters diminish along the ZnLi∅–*Q* series (with the exception of *a*, which is constant but, as indicated above, practically insensitive to the occupation of the *A* position) speaks also in favor of the above conclusion. Similar calculations as above, but done in a reverse sequence, prove that the compensation of the difference of 0.019 Å requires the radius of ∅ to be 0.667 Å, i.e., less than that of Li^+ by 0.061 Å.

Analogous calculations performed in terms of Shannon's ionic radii r_s give $r_\emptyset = 0.747$ Å and $r_{Li^+} - r_\emptyset = 0.013$ Å. Thus, the conclusion concerning the size of ∅ is qualitatively the same, independently of the set of the ionic radii used.

Using the simplified rules expressed in (i), (ii), and (iii), the ionic radii r_z and r_s and assuming that ∅ is smaller by 0.061 or 0.013 Å, respectively, as compared to the radius of the exhausted cation, the expected changes in the lattice parameters of ZnLi, MnLi, Zn∅, Mn∅, and Co∅, corresponding to the substitution of 0.1 Mo^{6+} for 1.0 V^{5+} are calculated and included in Table IV.

The experimental values of $\Delta a_{0.1}$ from Table IV are positive and nearly the same for all considered solid solutions independent of the Me/Li/∅ content (only MnLi makes a minor exception). They are moreover close to the $\Delta a_{0.1}$ values predicted by calculations in which the size of a BO_6 octahedron is taken into account (point (ii)). This means that parameter *a* in the brannerite-type structure is indeed practically insensitive to the nature and size of *A* but it follows the changes of BO_6 size dependent on the Mo/V ratio.

The experimental values of $\Delta b_{0.1}$ are also positive, constant within ±15% for all considered solid solutions, and about three times higher than $\Delta a_{0.1}$. The $\Delta b_{0.1}$ values calculated from the BO_6 size are positive but about three times smaller than the experimental ones while those calculated from the AO_6 size are strongly negative. Similar to *a* this means that *b* in the brannerite-type structure is insensitive to *A* but follows the changes of BO_6 size dependent on the Mo/V ratio. Much higher experimental values of $\Delta b_{0.1}$ as compared to $\Delta a_{0.1}$ may be explained by taking into account that, first, anionic layers in brannerites are tightly packed in direction *b* and more loosely packed in direction *a*, and second, it results from the structures of MoO_3 (*34*) and V_2O_5 (*35*) that V^{5+} tolerates much shorter bonds to oxygen on its opposite sides as compared to Mo^{6+}; the lengths of the respective bonds in the indicated structures are 1.88 and 1.95 Å, the difference being twice as large as the difference be-

tween the ionic radii of Mo^{6+} and V^{5+}. Let us note, moreover, that the calculated edge–edge distance in AO_6 (A = Zn) is 3.00 Å while the experimental value resulting from the structure determination (*13*) is 3.53 Å. This means that along [010] the ions are much more loosely packed in AO_6 chains than in BO_6 chains. This is the reason that parameter b is strongly sensitive to the size of B and insensitive to A.

The experimental values of $\Delta c \sin \beta_{0.1}$ are differentiated along the series of studied solid solutions, dependent on the occupation of the A site and usually negative (except for ZnLi and Mn∅ at higher X). The $\Delta c \sin \beta_{0.1}$ values calculated from the sizes of AO_6 and BO_6 octahedra (point (iii)) and r_z reveal the proper trend but are irrationally small. A much better fit between the experimental and calculated $\Delta c \sin \beta_{0.1}$ is reached under the additional assumption that the BO_6 octahedron does not change its size in the considered direction in spite of Mo/V substitution. This assumption may be argued taking into account that the BO_6 octahedron is strongly distorted in the direction close to [001] due to the longest B–O(2) bond of 2.68 Å (in ZnV_2O_6) which offers enough space for Mo^{6+} to be localized inside without movement of O(2). If r_s are taken instead of r_z, the fit between experimental and calculated $\Delta c \sin \beta_{0.1}$ is worse, but the trend is qualitatively good provided that the above-mentioned additional assumption is admitted.

In view of the above considerations one can conclude that the changes in lattice parameters of the considered solid solutions can be qualitatively explained provided that both the ionic radii (plus the estimated size of cation vacancy) and the compactness of the lattice in various directions are taken into account. The lack of quantitative fit between experimental and calculated values of $\Delta p_{0.1}$ is partly due to the simplified approach as formulated in points (i), (ii), and (iii). On the other hand, it is also due to the fact that some deviations from Vegard's law are observed, especially for ZnLi and Mn∅.

Finally, let us concentrate our attention on the composition of the saturated brannerite-type solid solutions (cf. Introduction and Fig. 4). In spite of the fact that all matrices have practically identical anionic sublattices, X_{max} in Me∅ varies from 0 (Me = Mg, Cd) to 45 (Me = Mn). If the presence of Mo^{6+} is totally or partly compensated by Li^+ (MnLi∅, MnLi∅, ZnLi, ZnLi∅), the content of Me^{6+} in MeLi∅ may be much higher than $2X_{max}$ in the respective Me∅. These facts clearly point to the A (Me/Li/O) sublattice being mainly responsible for the solubility of defects (Mo^{6+} and ∅) in the MeLi∅ solid solutions as well as in Me∅, Li∅, and MeLi which are particular cases of MeLi∅.

It also seems of interest to compare the boundaries of the existence (X_{max}, Y_{max}) of MnLi∅ and ZnLi∅. The MnLi and ZnLi solutions between the end members MeV_2O_6 and $LiVMoO_6$ may be considered here as matrices adopting an excess of Mo^{6+}, compensated by cation vacancies. The solubilities of ∅ in the end member phases are Mn∅–45, Zn∅–15, and Li∅–16. It is striking that the phase boundary of MnLi∅ extending between Mn∅–45 and Li∅–16 is nearly linear while that of ZnLi∅ (between Zn∅–15 and Li∅–16) changes in a nonmonotonal manner. In particular it is seen in Fig. 4 that there are ZnLi–Y compositions that tolerate a considerably higher concentration of vacancies (up to $X_{max} \approx 30$ at $Y \approx 25$) than both end members (X_{max} = 15 and X_{max} = 16, respectively). Simultaneously (Fig. 6) ZnLi shows a strong, negative deviation from Vegard's law seen in the changes of c, $c \sin \beta$, and V with composition. The simultaneous presence of Zn^{2+} and Li^+ in the A position thus has, at Y of about 25, a synergistic influence on the stabilization of the brannerite-type lattice, due to which it is able to tolerate an

increased content of ∅. This is not the case with MnLi and MnLi∅, where the lattice parameters of MnLi closely follow Vegard's law and the phase boundary of MnLi∅ is practically linear.

Conclusions

In the previous works (*1–6*) we have described a number of solid solutions of MoO_3 and $MoO_3 + Li_2O$ in the brannerite-type matrices of bivalent metal vanadates MeV_2O_6 (*Me* = Mn, Co, Cu). In the present paper our studies are extended on the ZnV_2O_6–MoO_3–Li_2O system. The existence of the following solid solutions has been confirmed: Zn∅ = $Zn_{1-x}\emptyset_xV_{2-2x}Mo_{2x}O_6$, ZnLi = $Zn_{1-y}Li_yV_{2-y}Mo_yO_6$, and ZnLi∅ = $Zn_{1-x-y}\emptyset_xLi_yV_{2-2x-y}Mo_{2x+y}O_6$. Zn∅ exists in the range $0 \le x \le 0.15$. ZnLi is formed for $0 \le y \le 1$; at $y = 1$ we deal with $LiVMoO_6$ which is able to incorporate an excess of MoO_3, resulting in the formation of Li∅ = $Li_{1-x}\emptyset_xV_{1-x}Mo_{1+x}O_6$, $0 \le x \le 0.16$ (*9*). The boundary of the stability of ZnLi∅ is extended between the saturated Zn∅ ($x_{max} = 0.15$) and saturated Li∅ ($x_{max} = 0.16$); x_{max} of ZnLi∅ depends on y and attains the highest value, of about 0.30, at $y = 0.25$. The synergistic effect linked with the simultaneous presence of Zn^{2+} and Li^+, manifested by negative deviations from Vegard's law, increases the stability of the matrix and its stability to vacancies.

Partially resolved phase diagrams of the ZnO–V_2O_5–MoO_3 and ZnV_2O_6–$LiVMoO_6$–MoO_3 systems allow the conclusion among others that depending on the composition Zn∅ and ZnLi solid solutions melt at 590–645°C and 645–651°C, respectively. Over the border of the existence of Zn∅ or ZnLi∅, several areas may be distinguished in which such phases coexist as saturated Zn∅ or ZnLi∅, MoO_3, V_2MoO_8, and $ZnMoO_4$ and solid solution of MoO_3 in V_2O_5.

Comparative analysis of the dependence of lattice parameters of *Me*∅ and *Me*Li (*Me* = Mn, Co, Zn) on composition (due to the differentiation of sizes of dopant ions) leads to the conclusion that a and b are dependent on the Mo/V ratio and almost insensitive to the occupation of the original *Me* site, while c (or $c \sin \beta$) is practically sensitive only to the size of $Me^{2+}/Li^+/\emptyset$. Cation vacancies behave as ions of a radius smaller than that of the exhausted cation by about 0.6 Å.

Acknowledgments

The authors thank Dr. Roman Kozłowski for critically reading the manuscript, Mrs. Lidia Dziembaj for her kind assistance with the preparation of a number of samples, and Dr. Wiesława Ziółkowska from the Academy of Mining and Metallurgy, Krakow, for her kind assistance with chemical analyses.

References

1. R. Kozłowski, J. Ziółkowski, K. Mocała, and J. Haber, *J. Solid State Chem.* **35,** 1 (1980); Erratum **38,** 138 (1981).
2. J. Ziółkowski, R. Kozłowski, K. Mocała, and J. Haber, *J. Solid State Chem.* **35,** 297 (1980).
3. T. Machej, R. Kozłowski, and J. Ziółkowski, *J. Solid State Chem.* **38,** 97 (1981).
4. R. Kozłowski and K. Stadnicka, *J. Solid State Chem.* **39,** 271 (1981).
5. J. Ziółkowski, K. Krupa, and M. Mocała, *J. Solid State Chem.* **48,** 376 (1983).
6. K. Mocała, J. Ziółkowski, and L. Dziembaj, *J. Solid State Chem.* **56,** 84 (1985).
7. R. Ruh and A. D. Wadsley, *Acta Crystallogr.* **21,** 974 (1966).
8. H. N. Ng and C. Calvo, *Canad. J. Chem.* **50,** 3619 (1972).
9. J. Galy, J. Darriet, and B. Darriet, *C.R. Acad. Sci. Paris Ser. C* **264,** 1477 (1967).
10. B. Darriet and J. Galy, *Bull. Soc. Fr. Miner. Crystallogr.* **91,** 325 (1968).
11. P. Courty, H. Ajot, and C. Marcilly, *Powder Technol.* **7,** 21 (1973).
12. F. Y. Robb, W. S. Glaunsinger, and P. Courtine, *J. Solid State Chem.* **30,** 171 (1979).
13. J. Angenault, *Rev. Chim. Miner.* **7,** 651 (1970).
14. J. Angenault and A. Rimsky, *C.R. Acad. Sci. Paris Ser. C* **267,** 227 (1968).

15. G. D. ANDREETTI, G. CALESTANI, A. MONTERO, AND M. BETTINELLI, *Z. Kristallogr.* **168,** 53 (1984).
16. S. C. ABRAHAMS, *J. Chem. Phys.* **46,** 2052 (1967).
17. M. A. EICK AND L. KIHLBORG, *Acta Chim. Scand.* **20,** 1659 (1966).
18. Joint Committee, "Powder Diffraction Standards," 5-508.
19. N. STRUPLER AND A. MORETT, *C.R. Acad. Sci. Paris* **260,** 1971 (1965).
20. N. STRUPLER AND A. MORETT, *Ann. Chim.* **10,** 345 (1965).
21. A. BIELAŃSKI, K. DYREK, J. POŹNICZEK, AND E. WENDA, *Bull. Acad. Polon. Sci. Ser. Sci. Chim.* **19,** 507 (1971).
22. A. BIELAŃSKI AND M. NAJBAR, *Pol. J. Chem.* **52,** 883 (1971).
23. V. L. VOLKOV, C. S. TYNKATSCHEVA, A. A. FOTIEV, AND E. V. TKATSCHENKO, *Zh. Neorg. Khim.* **17,** 2803 (1972).
24. R. H. MUNCH AND E. D. PIERRON, *J. Catal.* **3,** 406 (1964).
25. M. A. EICK AND L. KIHLBORG, *Acta Chim. Scand.* **20,** 722 (1966).
26. L. M. PLYASOVA, G. A. ZENKOVETS, I. P. OLENKOVA, AND D. W. TARASOVA, *Izv. Sib. Otd. Akad. Nauk USSR Ser. Chim. Nauk* **9,** 97 (1980).
27. A. A. DAVYDOV, T. G. KUZNETSOVA, AND T. V. ANDRUSHKEVICH, *React. Kinet. Catal. Lett.* **30,** 173 (1986).
28. G. M. CLARK AND A. N. PICK, *J. Thermal Anal.* **7,** 289 (1975).
29. J. M. CHAPLINA, *Zh. Prikl. Chim.* **37,** 1835 (1964).
30. V. A. MAKAROV, A. A. FOTIEV, AND L. N. SEREBRYAKOVA, *Zh. Neorg. Khim.* **16,** 2849 (1971).
31. J. J. BROWN AND F. A. HUMMEL, *Trans. Brit. Ceram. Soc.* **64,** 419 (1965).
32. J. ZIÓŁKOWSKI, *J. Solid State Chem.* **57,** 269 (1985).
33. R. D. SHANNON, *Acta Crystallogr. Sect. A* **32,** 751 (1976).
34. L. KIHLBORG, *Arkiv. Kemi* **21,** 357 (1963).
35. H. G. BACHMANN, F. R. AHMED, AND W. H. BERNES, *Z. Kristallogr. Kristallgeometr. Kristallphys. Kristallchem.* **115,** 110 (1961).